



Heterostructure-strengthened metal-support interaction of single-atom Pd catalysts enabling efficient oxygen activation for CO and VOC oxidation

Bin Wang^a, Qilei Yang^b, Bing Li^b, Hongyuan Ma^a, Yue Xuan^a, Chuan Gao^b, Yanjie Liang^a, Kaihang Zhang^d, Qiaowan Chang^{c,e}, Osvaldo Broesicke^d, Houlin Wang^b, Dong Wang^{a,c,*}, Tao Luan^a, Kuihua Han^a, Chunmei Lu^a, John Crittenden^d

^a School of Energy and Power Engineering, Shandong University, Jinan 250061, China

^b School of Environment, Tsinghua University, Beijing 100084, China

^c Department of Chemical Engineering, Columbia University, New York, NY 10027, USA

^d School of Civil and Environmental Engineering and the Brook Byers Institute for Sustainable Systems, Georgia Institute of Technology, 828 West Peachtree Street, Atlanta, GA 30332, USA

^e The Gene and Linda Voiland School of Chemical Engineering and Bioengineering, Washington State University, Pullman, WA 99164, USA

ARTICLE INFO

Keywords:

Air pollution control
Volatile organic compounds
Toluene oxidation
Catalytic combustion
Oxygen species

ABSTRACT

Catalytic oxidation of air pollutants depends on the active oxygen species, which requires a deep understanding of the active sites responsible for oxygen activation. In this study, we utilized a heterostructured support ($\text{ZnMn}_2\text{O}_4/\text{MnO}_2$) to modulate the metal-support interactions (MSIs) in single-atom Pd catalysts, achieving efficient activation of both adsorbed oxygen (O_{ads}) and lattice oxygen (O_{latt}). Specifically, the tailored MSIs induced an efficient redox pair for CO oxidation, i.e., Pd_1O_3 and Pd_1O_5 , promoting the activation of O_2 to O_{ads} , which led to 90% CO conversion at room temperature and a novel “MvK-induced L-H” reaction mechanism. Moreover, the tailored MSIs induced the stretching of the Mn-O bond, facilitating the participation of O_{latt} in toluene oxidation. Our results demonstrate a novel approach to modulating MSIs in single-atom catalysts (SACs) and highlight the superiority of the strong MSIs introduced by heterostructured supports for oxygen activation.

1. Introduction

The activation and generation of oxygen species (O_{ads} and O_{latt}) play a central role in numerous pivotal catalytic reactions. These reactions include the catalytic degradation of air pollutants such as carbon monoxide (CO) and volatile organic compounds (VOCs), the synthesis of value-added organic compounds, and the oxygen reduction reaction (ORR) in fuel cells.[1–6] Oxygen vacancy (O_{vac}) facilitates the conversion of gaseous O_2 into active O_{ads} via electron transfer from the surface to the adsorbent.[7,8] However, exposure to air or high temperature can cause O_{vac} to heal, thereby depriving the catalyst of O_{ads} . [9,10] The solid solution created by heteroatom doping is beneficial for activating O_{latt} . [11] Nevertheless, there is still a lack of effective methods to simultaneously introduce active O_{ads} and O_{latt} . The facile and efficient activation of oxygen species remains the bottleneck of catalytic oxidation.[4]

The use of SACs presents a promising approach for activating O_{ads} or O_{latt} of metal oxides.[12] For example, the negatively charged Au single

atoms in the Au_1/CuO SAC can generate defective oxygen sites by controlling the depletion of adjacent oxygen atoms, leading to the activation of gaseous O_2 to O_{ads} . [13] Similarly, Na single atoms transfer electrons to the support, resulting in O_{latt} with higher electron density and higher mobility.[14] It is worth noting that the activation of oxygen species by SACs is highly dependent on the strength of MSIs. Numerous studies have focused on modulating MSIs to enhance catalytic efficiency. [15,16] For instance, the Pd/CeO_2 system exhibits high activity towards CO oxidation, which is attributed to the strong MSIs that determine the anchoring and coordination environment of Pd species.[17–19] Conversely, the Pt_1/CeO_2 SAC shows low CO oxidation activity due to the weak MSIs, which can be enhanced by reducing Pt single atoms into clusters.[19–22] This strengthens MSIs and significantly enhances the catalytic activity, as CO oxidation occurs at the metal-support interface. [23] Hence, strong MSIs are essential for the activation of oxygen species in Pd or Pt SACs. Despite these advances, the facile synthesis of the single-atom Pd catalysts with strong MSIs and a comprehensive

* Corresponding author at: School of Energy and Power Engineering, Shandong University, Jinan 250061, China.

E-mail address: dwang@sdu.edu.cn (D. Wang).

<https://doi.org/10.1016/j.apcatb.2023.122753>

Received 29 November 2022; Received in revised form 24 March 2023; Accepted 9 April 2023

Available online 11 April 2023

0926-3373/© 2023 Elsevier B.V. All rights reserved.

understanding of their activation mechanism towards oxygen species remain a current challenge.

The SACs with Pd single atoms anchored in the oxide lattice exhibit stronger MSIs than those with Pd single atoms dispersed on the surface because the Pd single atoms of the latter are not fully coordinated with the O_{latt} of the support. The embedding of noble metal atoms promotes the orbital hybridization between metal atoms and oxide substrates, thereby affecting the catalytic behavior of SACs.[24,25] Previous study has demonstrated that anchoring Pd^{2+} in the CeO_2 lattice strengthens MSIs and forms ordered arrays of O_{vac} , thereby enhancing the catalytic activity of methane oxidation compared to the counterpart with Pd^{2+} dispersed on the CeO_2 surface.[26] Additionally, the incorporation of PdO_x species into the Co_2NiO_4 lattice effectively modifies the electronic structure of the catalyst, promoting electron transfer and activating adjacent O_{latt} in Co-O-Ni hybridization, thereby inducing substantially elevated O_{latt} activity for methane oxidation.[27] However, many catalytic reactions require the synergistic participation of O_{ads} (or O_{vac}) and O_{latt} , such as the ORR and catalytic oxidation of air pollutants. Hence, we cannot help but ponder whether we can further strengthen the MSIs of Pd SACs on this basis. If possible, O_{latt} may be activated concurrently with the activation of gaseous O_2 by O_{vac} .

Similar to the non-innocent ligands in homogeneous catalysis, the role of supports in catalysts cannot be ignored. Supports not only stabilize single atoms but also modify the physicochemical properties of the catalyst and can even participate in the catalytic cycle.[28,29] Recently, the interfacial hybrid strategies in support have been shown to effectively enhance the catalytic activity of CO oxidation through the interface-mediated Mars-van Krevelen (MvK) mechanism and improved dispersion of noble metals on the heterostructured support.[30] This suggests that the heterostructured support may strengthen the MSIs between the support and Pd single atoms. Moreover, the mechanism through which the as-induced strong MSIs affect Pd single atoms and supports may offer novel prospects for the advancement of SACs and thus merits further investigation.

Here we present a straightforward and effective approach for strengthening the MSIs between the ZnMn_2O_4 support and incorporated Pd^{2+} single atoms. The acid etching of the ZnMn_2O_4 support leads to the formation of a $\text{ZnMn}_2\text{O}_4/\text{MnO}_2$ heterostructure that strengthens MSIs, thereby inducing a unique coordination configuration of Pd^{2+} single atoms and stretched Mn-O bonds. The resulting Pd_1O_3 and Pd_1O_5 species form an exceedingly efficient redox pair that rapidly cycles between activating gaseous O_2 and being reduced by CO. This leads to 90% CO conversion at room temperature during CO oxidation and the discovery of a novel "MvK-induced L-H" reaction mechanism. The stretched Mn-O bond exhibits higher O_{latt} activity, which significantly reduces the energy barrier for toluene oxidation. The tuning of MSIs to activate oxygen species is not limited to CO and toluene oxidation, which are the primary model substrates used in this study.

2. Experimental section

2.1. Materials preparation

All the reagents used in the synthesis process are analytical-grade and do not require further purification before use.

The synthesis method of ZMO involves several steps. Firstly, 6.22 g of $\text{Zn}(\text{NO}_3)_2 \cdot 6\text{H}_2\text{O}$, 14.96 g of $\text{Mn}(\text{NO}_3)_2$ 50% solution, and 19.76 g of $\text{C}_6\text{H}_8\text{O}_7 \cdot \text{H}_2\text{O}$ (citric acid) are dissolved in 100 mL of deionized water and stirred at room temperature overnight. Secondly, the resulting solution is heated in a water bath at 60 °C until it becomes viscous and foamy, forming a wet gel. Thirdly, the wet gel is dried at 150 °C overnight to form a dry gel. Finally, the dry gel is calcined in a muffle furnace at a rate of 1 °C·min⁻¹, heated to 500 °C, and calcined for 4 h to obtain the ZMO catalyst.

The synthesis method of PZMO is similar to that of ZMO. In this case, 0.06 g of $\text{Pd}(\text{NO}_3)_2 \cdot 2\text{H}_2\text{O}$ is added to the mixture of 6.15 g of Zn

$(\text{NO}_3)_2 \cdot 6\text{H}_2\text{O}$, 14.96 g of $\text{Mn}(\text{NO}_3)_2$ 50% solution, and 19.76 g of $\text{C}_6\text{H}_8\text{O}_7 \cdot \text{H}_2\text{O}$ dissolved in 100 mL of deionized water. The remaining steps are identical to those of ZMO.

The synthesis method of ZMO-30 involves the acid etching of the ZMO precursor using dilute HNO_3 for 30 min. First, 1 g of ZMO is added to 150 mL of 1 M HNO_3 and vigorously stirred at room temperature for 30 min. Second, the resulting suspension is filtered and washed until the pH of the filtrate is close to 7. Third, the precipitate is dried at 80 °C overnight. Finally, the sample is calcined in a muffle furnace at a rate of 1 °C·min⁻¹, heated to 350 °C, and calcined for 2 h to obtain the ZMO-30 catalyst.

The synthesis method for other catalysts, such as ZMO-20, ZMO-40, ZMO-720, PZMO-30, and PZMO-720, is similar to that of ZMO-30, except for the use of different precursors and acid etching times.

The Pd/ZMO-30 catalyst is synthesized using the incipient wetness impregnation method. After impregnation, the sample is dried overnight at 80 °C and further calcined in a muffle furnace at a rate of 1 °C·min⁻¹, heated to 350 °C, and calcined for 2 h to obtain the Pd/ZMO-30 catalyst.

2.2. Catalysts characterization

The catalysts are characterized by X-ray diffraction (XRD), Brunauer-Emmett-Teller (BET), transmission electron microscopy (TEM), aberration-corrected scanning transmission electron microscope (AC-STEM), high-angle annular dark field-scanning transmission electron microscopy (HAADF-STEM), energy-dispersive X-ray spectroscopy (EDX), electron energy loss spectroscopy (EELS), X-ray photoelectron spectroscopy (XPS), electron paramagnetic resonance (EPR), inductively coupled plasma-optical emission spectroscopy (ICP-OES), CO chemisorption, X-ray absorption spectra (XAS), hydrogen temperature-programmed reduction (H_2 -TPR), oxygen temperature-programmed desorption (O_2 -TPD), ammonia temperature-programmed desorption (NH_3 -TPD), in situ pyridine-Fourier transform infrared (in situ pyridine-FTIR), in situ diffuse reflectance infrared Fourier transform spectra (in situ DRIFTS), and in situ Raman. Detailed information about the instruments and their operating conditions are described in the [Supporting Information](#).

2.3. Catalytic performance

The catalytic performance of CO and toluene oxidation is evaluated in a fixed-bed microreactor with a 0.10 g catalyst (40–60 mesh). A gas chromatograph (Agilent 7890 A) is used to monitor the concentrations of toluene, CO, and CO_2 . The detailed descriptions of the reaction conditions, CO_2 yield, and apparent activation energy are presented in the captions of [Figs. 4, 5, 6](#), and [Supporting Information](#).

3. Results

3.1. Synthesis and physicochemical characteristics

[Fig. 1A](#) shows the uniform dispersion of three metal salt precursors (Zn, Mn, and Pd) in a citric acid solution. The resulting gel is pyrolyzed in the air at 500 °C to obtain ZnMn_2O_4 spinel with Pd^{2+} single atoms embedded in its lattice, denoted as "PZMO". The pure ZnMn_2O_4 spinel without Pd^{2+} single atoms is referred to as "ZMO". Subsequently, we treat the PZMO catalyst with dilute nitric acid for 30 min to obtain "PZMO-30", where "30" represents the treatment time (min). Likewise, the "ZMO-30" catalyst is synthesized in the same manner, except that the acid-treated precursor is changed to ZMO. In an acidic environment, Zn^{2+} ions will dissolve from the ZnMn_2O_4 framework, resulting in the formation of MnO_2 , as reported in our recent work.[31] By controlling the acid treatment time, we retain a portion of the Zn^{2+} ions in the ZnMn_2O_4 framework, thereby facily obtaining the $\text{ZnMn}_2\text{O}_4/\text{MnO}_2$ heterostructure with a core-shell-like morphology in ZMO-30 and PZMO-30. Notably, Pd^{2+} is practically insoluble in dilute HNO_3 solution,

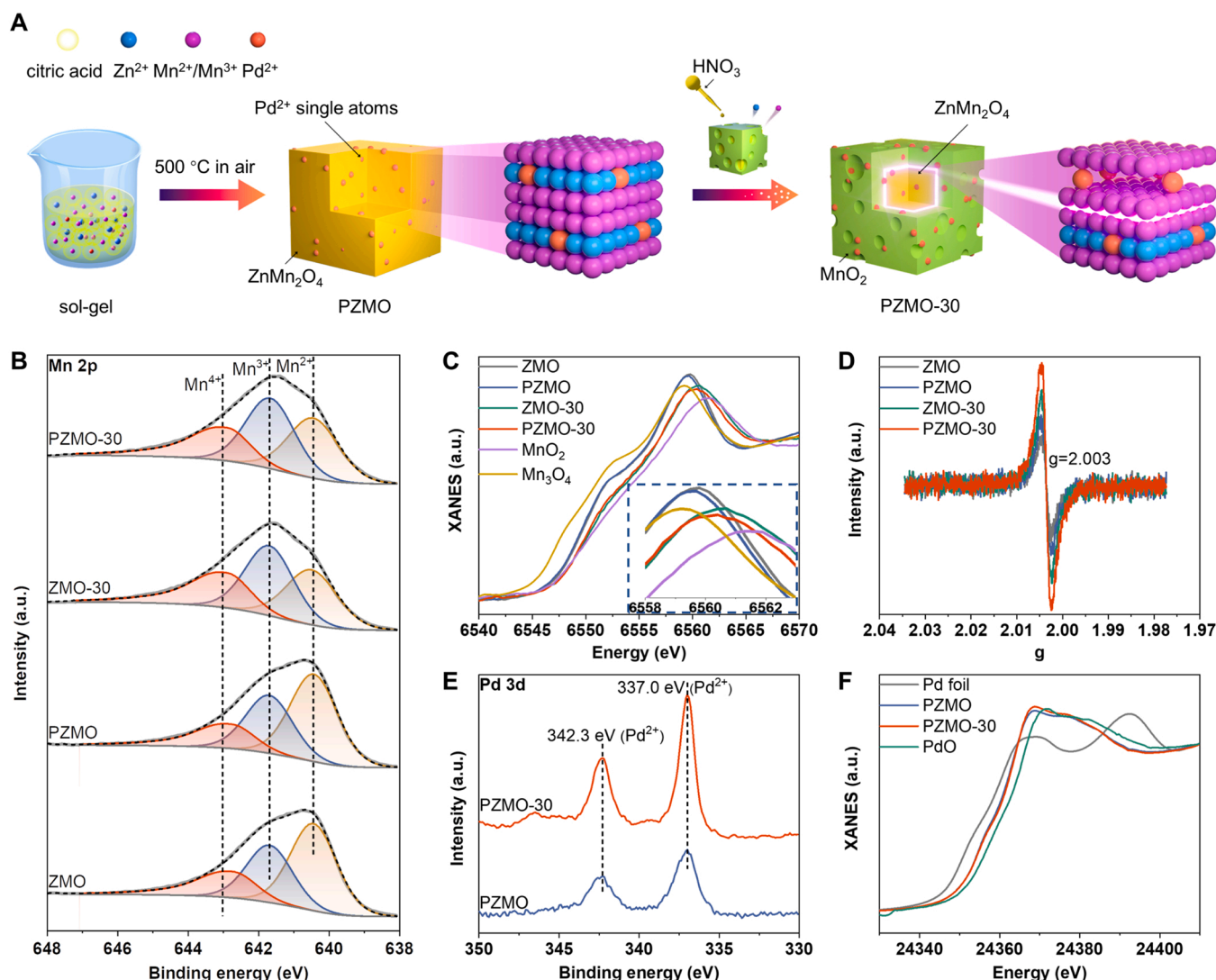


Fig. 1. Catalyst synthesis and physicochemical characterizations. (A) Schematic illustration for the synthesis process and structural characteristics of PZMO and PZMO-30. (B) XPS spectra of Mn 2p. (C) XANES spectra at the Mn K-edge. (D) EPR spectra. (E) XPS spectra of Pd 3d. (F) XANES spectra at the Pd K-edge.

ensuring that the Pd^{2+} species remain atomically dispersed within the lattice of PZMO-30.

Table S1 shows the Pd loadings of PZMO and PZMO-30 to be 0.49 wt % and 0.90 wt%, respectively, as determined by ICP-OES. Fig. S2 illustrates a decrease in the surface concentration of Zn^{2+} in ZMO-30 and PZMO-30. Detailed information on the surface concentration of metal elements, detected using XPS, is presented in Table S2. The surface Mn/Zn molar ratios of ZMO-30 and PZMO-30 are considerably higher than the corresponding ICP-OES results, indicating that their surface compositions differ from the bulk, and heterostructures form as a result. Moreover, the AC-STEM equipped with EDX is employed to investigate the element mapping of PZMO-30 (Fig. 2E), which suggests that surface Zn is etched by HNO_3 , while Mn is homogeneously distributed from the surface to the bulk, further validating the formation of heterostructures. In contrast, the distribution of Zn and Mn in PZMO is uniform (Fig. S9).

The XRD patterns (Fig. S3) demonstrate that a MnO_2 (111) diffraction peak is present in the ZMO-30 and PZMO-30 catalysts. This indicates that the acid treatment introduces a MnO_2 shell on the ZnMn_2O_4 surface. The BET results (Table S3) reveal that ZMO-30 and PZMO-30 exhibit larger surface areas (68.9 and $64.5 \text{ m}^2\cdot\text{g}^{-1}$, respectively) in comparison to ZMO and PZMO (51.2 and $44.7 \text{ m}^2\cdot\text{g}^{-1}$, respectively). The porous structure induced by acid treatment in ZMO-30 makes it a suitable support for Pd single atoms. Moreover, this structure enables Pd

single atoms embedded in the lattice to participate in the catalytic reaction to the greatest extent.

The dissolution of Zn^{2+} ions and the subsequent exposure of more B-site cations (Mn^{n+}) lead to an enrichment of Lewis acid sites on the catalyst surface.[32,33] Therefore, we use pyridine-FTIR to further investigate the changes in the surface properties of the catalysts. Fig. S4 illustrates that the strength of Lewis acid sites is weaker compared to that of Brønsted acid sites. The total amount of acid sites, determined semi-quantitatively by pyridine-FTIR analysis (Fig. S5 and Table S4), follows the order: PZMO-30 > ZMO-30 > ZMO > PZMO. This order is consistent with the quantitative analysis obtained from the NH_3 -TPD results (Fig. S6 and Table S4). PZMO-30 has the highest concentration of Lewis acid sites ($29.3 \text{ mmol}\cdot\text{g}^{-1}$) compared to ZMO-30 ($21.9 \text{ mmol}\cdot\text{g}^{-1}$), PZMO ($11.1 \text{ mmol}\cdot\text{g}^{-1}$), and ZMO ($14.2 \text{ mmol}\cdot\text{g}^{-1}$). Comparing ZMO and ZMO-30, HNO_3 etching of Zn^{2+} (A-site of ZnMn_2O_4 spinel) results in more B-site Mn^{n+} on the surface of ZMO-30, which act as Lewis acid sites. Comparing ZMO-30 and PZMO-30, PZMO-30 has more Lewis acid sites, suggesting that, in addition to Mn^{n+} , PZMO-30 may contain more O_{vac} , which also serve as Lewis acid sites in metal oxides.[34,35].

To reveal the O_{vac} concentration and electronic structure properties of the catalysts, we first collect the XPS spectra of Mn 2p (Fig. 1B). Table S5 shows that ZMO-30 and PZMO-30 have significantly higher

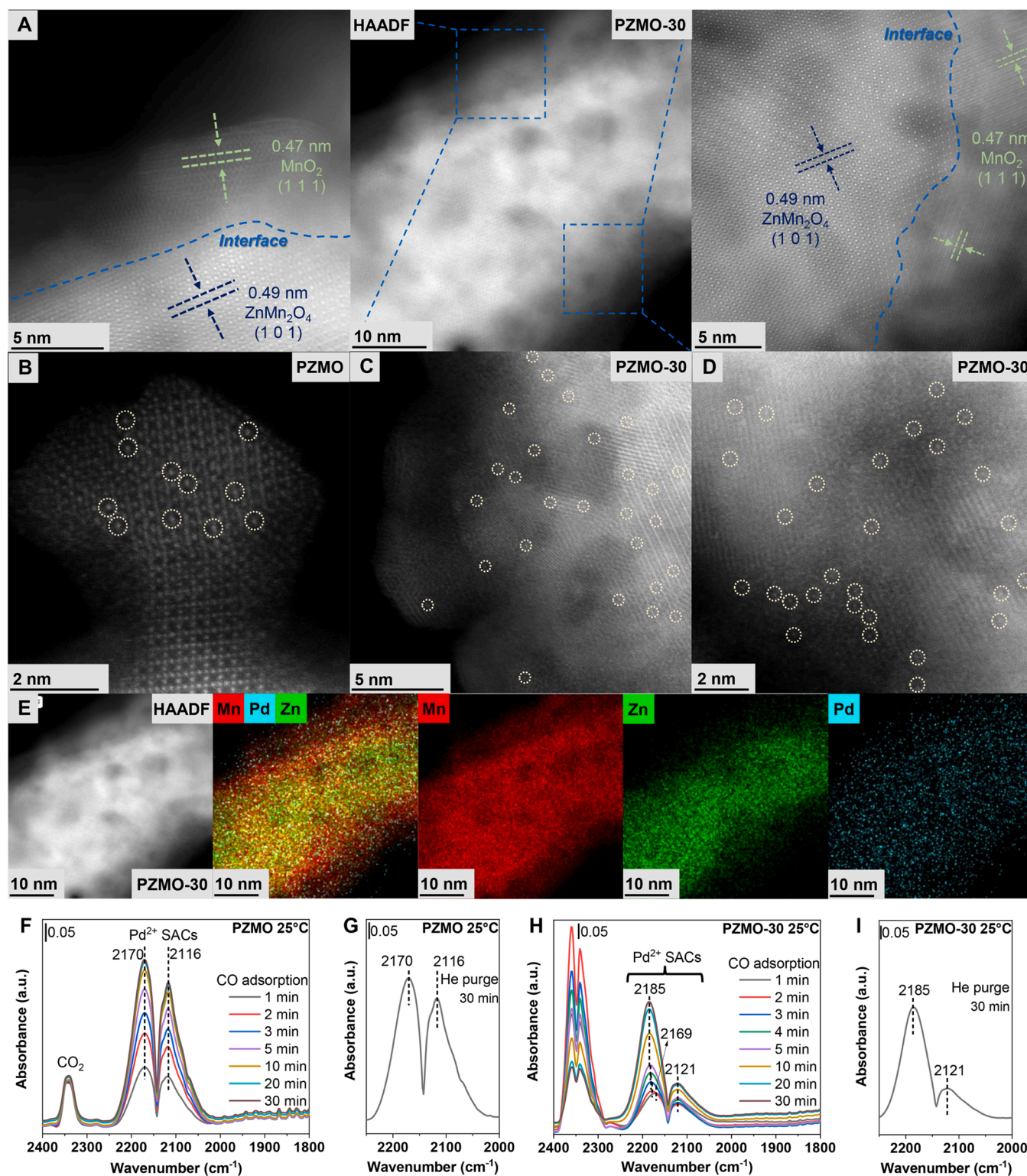


Fig. 2. The observation of heterostructured support and determination of Pd²⁺ single atoms. HAADF-STEM images of (A) the heterostructure in PZMO-30, the Pd²⁺ single atoms of (B) PZMO and (C, D) PZMO-30, and the (E) corresponding EDX mapping of Mn, Pd, and Zn. (F) In situ DRIFTS over PZMO under CO adsorption condition (1% CO, He balance, 25 °C) followed by (G) purging in He at 25 °C. (H) In situ DRIFTS over PZMO-30 under CO adsorption condition (1% CO, He balance, 25 °C) followed by (I) purging in He at 25 °C.

Mn⁴⁺ ratios compared to ZMO and PZMO, which also confirms that the acid treatment induces the formation of the MnO₂ shell. Further, XAS is conducted to understand the oxidation states of Mn. In Fig. 1C, Mn K-edge X-ray absorption near edge structure (XANES) spectra are presented. The white lines of PZMO-30 and PZMO shift to lower energy

than ZMO-30 and ZMO, respectively, indicating that the doping of Pd species slightly reduces the oxidation state of Mn cations. Thus, the oxidation states of Mn cations follow the sequence of MnO₂ > ZMO-30 > PZMO-30 > ZMO > PZMO > Mn₃O₄, implying that PZMO-30 and PZMO have more O_{vac} than ZMO-30 and ZMO, respectively. Then, we

conduct EPR experiments to probe the relative content of O_{vac} (Fig. 1D) and find that the content of O_{vac} follows the sequence of $PZMO-30 > ZMO-30 > PZMO > ZMO$, consistent with Mn K-edge XANES spectra.

The XPS spectra of Pd 3d (Fig. 1E) are collected to understand the oxidation states of Pd in PZMO and PZMO-30. The binding energy at 337.0 and 342.3 eV corresponds to oxidized Pd^{2+} . [27] Further, Pd K-edge XANES spectra (Fig. 1F) indicate that compared to Pd foil, PZMO and PZMO-30 show similar absorption threshold energies with that of PdO, indicating a bivalent state (Pd^{2+}) of Pd species. [36].

The TEM image in Fig. S7 reveals the cobblestone morphology of ZMO and PZMO. Upon acid treatment, the edges of the cobblestones become blurred, resulting in a loose pore structure. This morphology is beneficial as it facilitates the contact of reactants with active sites. Further, a careful observation of a cobblestone nanoparticle of PZMO-30 using AC-STEM in the HAADF imaging mode, as shown in Fig. 2A, reveals the presence of $ZnMn_2O_4$ (101) core and MnO_2 (111) shell, without any trace of Pd/PdO nanoparticles or large clusters. Moreover, lattice fringe blurring is evident at the interface, indicating possible alterations in catalytic properties due to interfacial interactions.

The atomic dispersion of Pd in PZMO and PZMO-30 is verified through HAADF images (Fig. 2B, C, and D), with bright spots highlighted by bright yellow circles being attributed to Pd^{2+} single atoms. In PZMO, Pd^{2+} single atoms are present in the $ZnMn_2O_4$ lattice (Fig. 2B), occupying Zn^{2+} sites. Additional evidence is provided in Fig. S8. EDX analysis (Fig. 2E and Fig. S9) demonstrates that the distribution of Pd^{2+} is uniform, confirming that Pd^{2+} is atomically dispersed in both PZMO and PZMO-30. Further, we use in situ DRIFTS of CO adsorption at 25 °C to probe Pd species over PZMO and PZMO-30 (Fig. 2F-I). The CO absorption observed beyond 2250 cm^{-1} is attributed to gaseous CO_2 . [37] The PZMO (Fig. 2G) and PZMO-30 (Fig. 2I) catalysts demonstrate CO adsorption within the 2200–2100 cm^{-1} range, which corresponds to linear adsorption of CO on Pd^{2+} sites ($CO-Pd_1$). [36,38,39] Additionally, no CO adsorption is detected within the 2000–1900 or < 1900 cm^{-1} ranges, which are associated with bridged ($CO-Pd_2$) and threefold hollow ($CO-Pd_3$) configurations, respectively. [40] These findings provide further evidence that the Pd species in both PZMO and PZMO-30 exist as Pd^{2+} single atoms. The synchrotron radiation technique provides conclusive evidence of Pd^{2+} single atoms. The XANES spectra of PZMO and PZMO-30 (Fig. 1F) exhibit a distinct edge feature that differs from that of PdO, implying that the coordination geometries of Pd species in PZMO and PZMO-30 differ from PdO. [36] The analysis of extended X-ray absorption fine structure (EXAFS, shown in Fig. 4A) reveals the absence of Pd-Pd shell in PZMO and PZMO-30, which is evident in Pd foil and PdO, thereby conclusively confirming the atomic dispersion of Pd^{2+} in both PZMO and PZMO-30. The peak around 3.4 Å cannot be assigned to Pd-Pd, as Pd-Pd does not exist in PZMO and PZMO-30. Given that Pd^{2+} single atoms replace Zn^{2+} in PZMO and the distance of Zn-Mn (Zn-O-Mn) in $ZnMn_2O_4$ spinel is approximately 3.401 Å, we attempt to assign the peak near 3.4 Å to Pd-Mn (Pd-O-Mn) for fitting. The best-fitting results are presented in Fig. S10 and Table S6. The coordination number (CN) of Pd-Mn in PZMO and PZMO-30 is close to 8, which is close to saturation coordination, confirming that Pd^{2+} single atoms are embedded in the lattice of PZMO and PZMO-30, replacing Zn^{2+} . The CO chemisorption experiments (Table S1) show that 7.14% and 4.07% of Pd^{2+} single atoms exist in the surface lattice in PZMO and PZMO-30, respectively, while the rest are dispersed in the bulk phase. It is noteworthy that the content of Pd^{2+} single atoms in the surface lattice in PZMO and PZMO-30 is nearly equivalent, owing to the higher Pd loading in PZMO-30 ($4.07\% \times 0.90/0.49 = 7.48\%$).

3.2. MSIs effect on oxygen species

The embedded Pd^{2+} single atoms may strengthen MSIs, which induces charge redistribution and facilitates the activation of oxygen species. The reactivity of oxygen species plays a critical role in catalytic

oxidation performance. The EPR results (Fig. 1D) demonstrate that acid treatment endows ZMO-30 and PZMO-30 with more O_{vac} , which should be attributed to the $ZnMn_2O_4@MnO_2$ heterostructure. Therefore, we use the EELS multi-spot scanning technique to investigate the chemical states of Mn and O near the $ZnMn_2O_4@MnO_2$ interface. The annular dark-field (ADF) image and the corresponding Mn $L_{2,3}$ -edge and O K-edge spectra are shown in Fig. S11. As summarized in Fig. 3A, there is redundant coordinating oxygen with high O_{latt} mobility at the interface compared to the $ZnMn_2O_4$ side, [41] while there are more O_{vac} at the interface compared to the MnO_2 side. [34] This finding indicates that the $ZnMn_2O_4@MnO_2$ heterostructure realizes the synergistic activation of O_{ads} and O_{latt} through the interface effects between $ZnMn_2O_4$ and MnO_2 . Notably, this effect is not observed in PZMO (Fig. S12), thus confirming that the observed enhancement is a result of the $ZnMn_2O_4@MnO_2$ heterostructure.

The H_2 -TPR experiment (Fig. 3B) provides valuable insights into the O_{latt} mobility in a reducing atmosphere, which is critical for catalytic oxidation. In the case of ZMO, the H_2 -TPR curve exhibits only one reduction peak at 389 °C, which is attributed to the reduction of Mn^{3+} to Mn^{2+} . For ZMO-30, two reduction peaks are observed at 185 °C and 373 °C, which are attributed to the reduction of Mn^{4+} to Mn^{3+} and Mn^{3+} to Mn^{2+} , respectively. [31] As for PZMO, a weak peak at 110 °C is attributed to the reduction of Pd^{2+} single atoms, and the peak at 181 °C is attributed to the reduction of Mn^{3+} to Mn^{2+} . [42] The embedded Pd^{2+} single atoms in the $ZnMn_2O_4$ lattice significantly reduce the reduction temperature of Mn^{3+} in PZMO due to the strong interactions between Pd^{2+} single atoms and $ZnMn_2O_4$. For PZMO-30, the reduction temperatures of Mn^{4+} and Mn^{3+} are further reduced and even coincide with the reduction peak of Pd^{2+} single atoms. This suggests that Pd^{2+} single atoms can activate the O_{latt} of PZMO and PZMO-30, with a stronger activation effect observed in PZMO-30 because the $ZnMn_2O_4@MnO_2$ heterostructure strengthens the MSIs. The H_2 -TPR results indicate that the properties of Pd^{2+} single atoms in PZMO and PZMO-30 differ from each other, highlighting the role of the $ZnMn_2O_4@MnO_2$ heterostructure in enhancing the interaction effect of support on Pd^{2+} single atoms, and in turn the interaction effect of Pd^{2+} single atoms on the O_{latt} of support Figs. 4, 5, 6.

The XPS spectra of O 1s (Fig. 3C) are analyzed to determine the relative content of O_{ads} and O_{latt} . Two peaks are observed, corresponding to O_{latt} (529.6–529.8 eV) and O_{ads} (531.3 eV). [43] The relative content of O_{ads} is found to be in the order of $PZMO-30 > ZMO-30 > PZMO > ZMO$ (Fig. 3E). The O_2 -TPD experiment is used to investigate the desorption of oxygen species from the catalyst surface. The desorption peaks below 300 °C are assigned to O_{ads} , while those between 300 and 600 °C are assigned to O_{latt} (Fig. 3D). [44] Fig. 3E shows the amount of O_2 desorption from the catalysts. PZMO-30 exhibits a higher amount of O_{latt} compared to ZMO-30, indicating that the Pd^{2+} single atom in PZMO-30 has a significant activation effect on the O_{latt} of the support. This effect is not observed for ZMO and PZMO. On the other hand, Pd^{2+} -containing samples (PZMO and PZMO-30) exhibit a higher amount of O_{ads} , indicating that Pd^{2+} single atoms contribute to O_{ads} . Notably, the Pd^{2+} single atoms in PZMO-30 induce a significantly higher increase in O_{ads} compared to that in PZMO, suggesting that the heterostructured support ($ZnMn_2O_4@MnO_2$) has a significant activation effect on Pd^{2+} single atoms.

The $ZnMn_2O_4@MnO_2$ heterostructure significantly strengthens the MSIs, the effect of which is critical to oxygen activation and catalytic properties. Therefore, we explore the interaction effect of the heterostructured support on Pd^{2+} single atoms for CO oxidation, and conversely, the interaction effect of Pd^{2+} single atoms on support for toluene oxidation in the latter two parts, respectively.

3.3. MSIs effect on Pd^{2+} single atoms

The EXAFS fitting results at Pd K-edge for PZMO and PZMO-30 (Fig. 4A and Table S6) indicate the Pd_1O_4 coordination of Pd^{2+} single

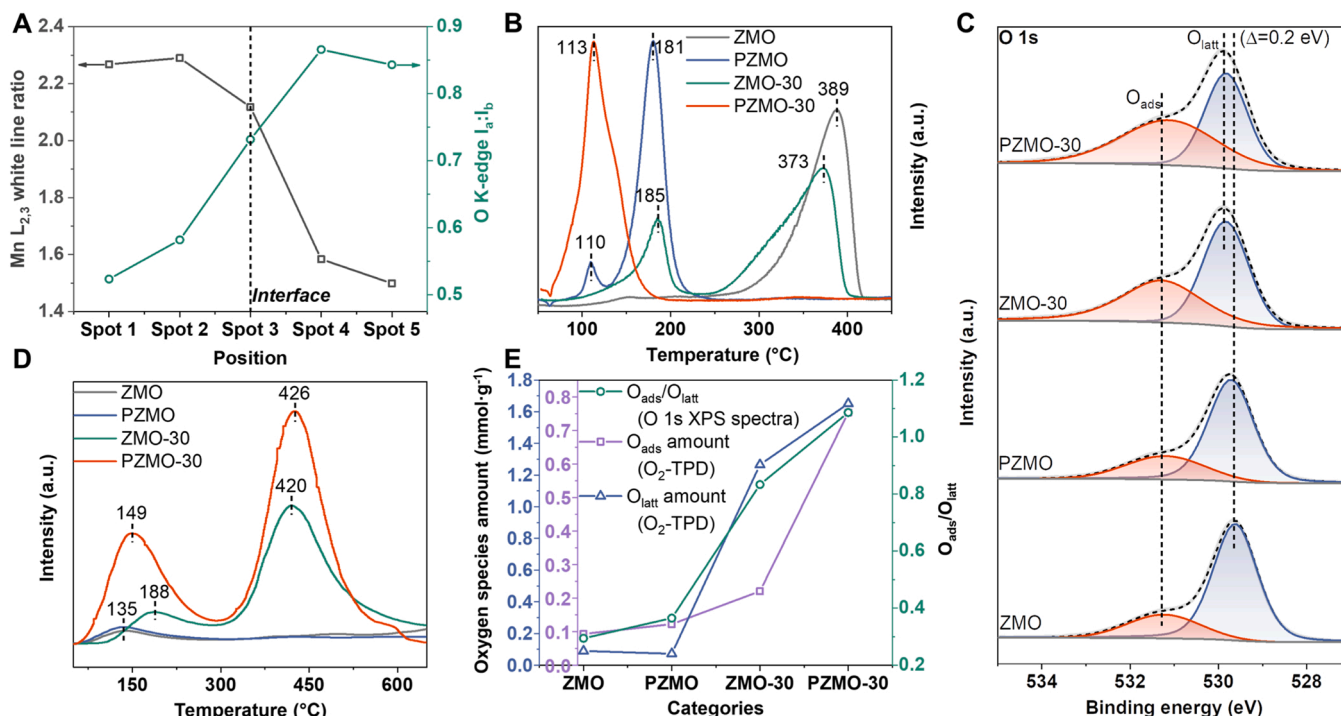


Fig. 3. The effect of the MSIs on oxygen species. (A) I_a:I_b of O K-edge prepeaks and Mn L_{2,3} white line ratio as functions of different positions on PZMO-30 (calculated from Fig. S11). (B) H₂-TPR profiles. (C) XPS spectra of O 1s (D) O₂-TPD profiles. (E) The amount of O_{ads} and O_{latt} calculated by the O₂-TPD results as well as the content ratio of O_{ads}/O_{latt} calculated by the XPS spectra of O 1s.

atoms. The only difference is the average Pd-O coordination number (CN), which is ~ 3.7 for PZMO and ~ 4.6 for PZMO-30. A coordination number of ~ 3.7 suggests that the Pd²⁺ single atoms in PZMO are close to saturated coordination, while a coordination number of ~ 4.6 indicates the presence of five-coordinated Pd²⁺ single atoms in PZMO-30. This result is consistent with the discovery of five-coordinated Pt₁O₅ by Kunwar et al. using EXAFS, who proposed that Pt₁O₃ can activate gaseous O₂ to form Pt₁O₅ after Pt₁O₄ lost one of its coordinated oxygens to form an O_{vac} (Pt₁O₃). [45,46] Gaseous O₂ is not dissociatively adsorbed on O_{vac}, but both the two oxygen atoms are bonded to Pt to form a five-coordinated motif. Similarly, the five-coordinated Pd₁O₅ was also discovered with a similar model and mechanism. [36] The presence of five-coordinated Pd₁O₅ in PZMO-30 indicates abundant O_{vac} and is consistent with the Mn K-edge XANES and EPR results. This finding explains why PZMO-30 possesses more O_{ads} in Fig. 3C and D, as the Pd²⁺ single atoms of PZMO-30 can activate gaseous O₂ to O_{ads} more efficiently.

The configuration of Pd²⁺ single atoms is studied using in situ DRIFTS of CO adsorption at 25 °C. In Fig. 2F and G, the peaks at 2116 and 2170 cm⁻¹ are assigned to the perfect Pd₁O₄ in the ZnMn₂O₄ lattice with almost saturated coordination. Fig. 2H and I show the in situ DRIFTS of PZMO-30 under the CO/He and He atmosphere, respectively. Unlike PZMO, where the peak intensity gradually increases with CO adsorption time, PZMO-30 shows a decrease in the peak intensity at 2121 cm⁻¹ and a shift of the peak at 2169 cm⁻¹ to higher wavenumbers, accompanied by a significant increase in the CO₂ peak intensity (much higher than that of PZMO) at 2 min. The peak intensity at 2121 cm⁻¹ gradually increases afterward, but the final intensity at 30 min is lower than that at 2116 cm⁻¹ of PZMO (Fig. 2F). Meanwhile, the peak at 2169 cm⁻¹ continues to shift to higher wavenumbers, eventually reaching 2185 cm⁻¹. In contrast to PZMO, the CO adsorption peak of Pd₁O₄ for PZMO-30 shifts from 2116 cm⁻¹ (perfect Pd₁O₄, as shown in Fig. 2F) to 2121 cm⁻¹, indicating that the ZnMn₂O₄@MnO₂ heterostructure induces the formation of distorted Pd₁O₄. [46] Compared to

perfect Pd₁O₄ (2116 cm⁻¹), the distorted Pd₁O₄ (2121 cm⁻¹) has weaker Pd-O bonds, making it more susceptible to being reduced by CO to Pd₁O₃ (2185 cm⁻¹) at room temperature. The reduction process from distorted Pd₁O₄ (2121 cm⁻¹) to Pd₁O₃ (2185 cm⁻¹) at 25 °C is evidenced by the decreased peak intensity of distorted Pd₁O₄ at 2121 cm⁻¹ compared with that of perfect Pd₁O₄ at 2116 cm⁻¹, the gradual shift of the peak at 2169 cm⁻¹ to higher wavenumbers (eventually shifting to 2185 cm⁻¹), and the significant increase in the CO₂ peak intensity. Note that the peak at 2169 cm⁻¹ at 1 min is asymmetric, suggesting that it may result from the combined superposition of the following two peaks: the peak at high wavenumber locates at 2185 cm⁻¹, as a symmetrical peak at 2185 cm⁻¹ forms after CO adsorption is saturated, while the peak position and assignment at low wavenumber require further investigation, and we will discuss this in detail later in this article. Additionally, the high CO₂ signal intensity at room temperature implies that PZMO-30 may catalyze CO oxidation at room temperature.

Low-temperature CO oxidation activity is accordingly evaluated. As a comparison, we extended the acid treatment time to 720 min to obtain the ZMO-720 and PZMO-720 catalysts. The XRD results (Fig. S13) show MnO₂ diffraction peaks for both ZMO-720 and PZMO-720, with no other phases observed. This indicates that almost all Zn²⁺ ions are dissolved (ICP-OES results in Table S1) and that Pd species in PZMO-720 are highly dispersed. The prolongation of acid treatment time further increases the surface area of ZMO-720 and PZMO-720 (Table S3), which should be related to the enrichment of pore structure. For PZMO-720, Pd species exist in the MnO₂ lattice in the form of Pd²⁺ single atoms (1.39 wt%) (Fig. S14 and Table S1). We also synthesized a Pd/ZMO-30 catalyst using ZMO-30 as support with similar Pd loadings as PZMO-30 (determined by ICP-OES in Table S1) using the incipient wetness impregnation method. No Pd species are detected by XRD (Fig. S13), and most of the Pd species are dispersed on the surface in the form of Pd²⁺ single atoms, although small amounts of clusters or nanoparticles are present (Fig. S15 and Table S1). The catalytic performance of CO oxidation to CO₂ and corresponding Arrhenius plots are shown in Table S7, Fig. 4B, and C. The presence of Pd²⁺ single atoms significantly

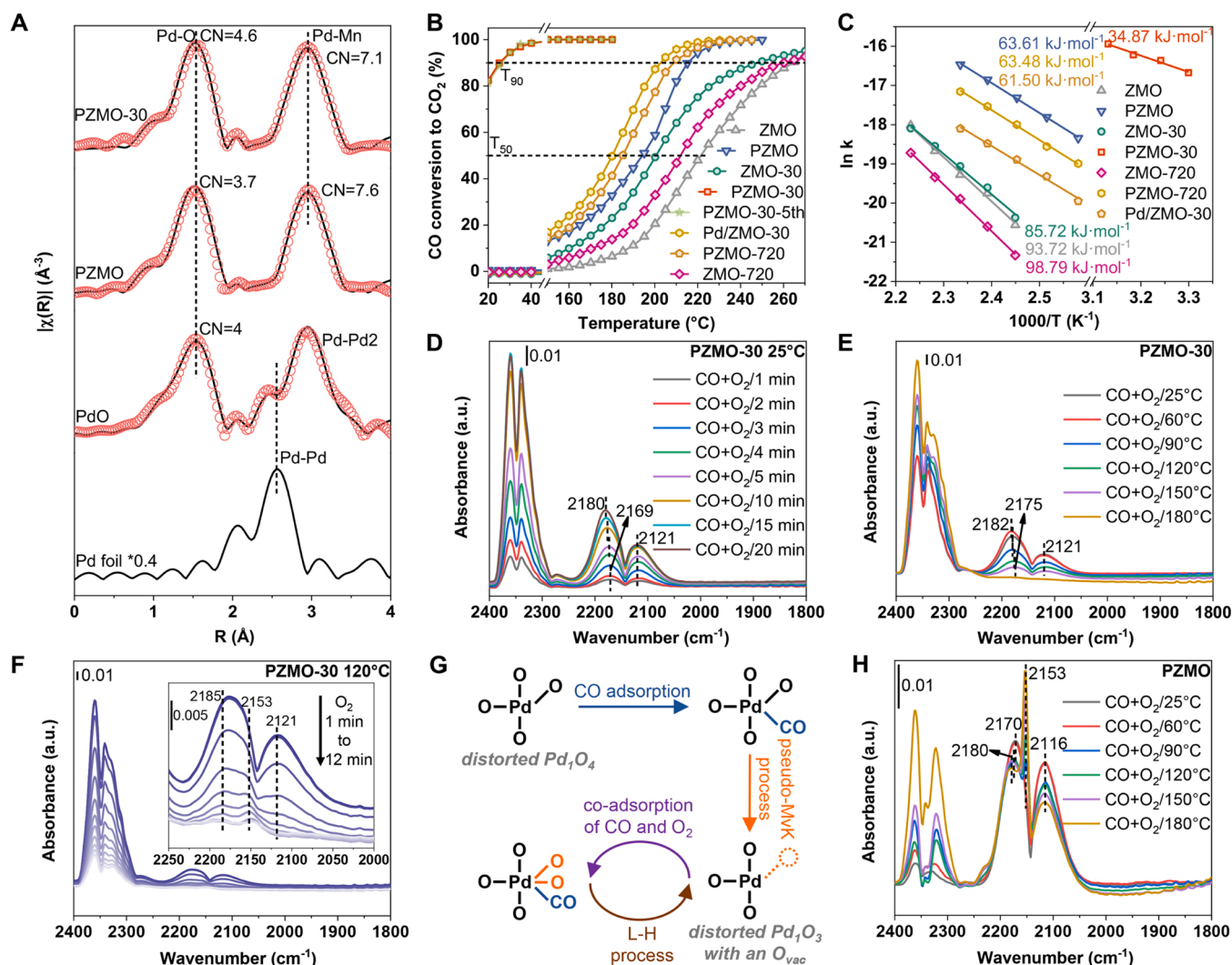


Fig. 4. The effect of the strong MSIs on Pd²⁺ single atoms. (A) Fourier-transformed K-edge EXAFS spectra in the R-space of Pd. (B) CO conversion to CO₂ as a function of temperature. Reaction conditions: A catalyst loading of 100 mg, 1% CO, and 20% O₂ in N₂ with a total flow rate of 100 mL·min⁻¹ under a gas-hourly space velocity (GHSV) of 60000 mL·g⁻¹·h⁻¹. (C) Arrhenius plots of the catalysts. In situ DRIFTS over PZMO-30 under CO oxidation condition (1% CO and 20% O₂, He balance) (D) at 25 °C, (E) during the gradual heating process, and (F) followed by purging in 20% O₂ in He at 120 °C. (G) Schematic illustration of CO oxidation mechanism on PZMO-30. (H) In situ DRIFTS measurements over PZMO under CO oxidation condition (1% CO and 20% O₂, He balance) during the gradual heating process.

enhances the catalytic activity of PZMO, PZMO-720, and Pd/ZMO-30, which should be due to the activation effect of Pd²⁺ on the CO molecules. The apparent activation energies of PZMO, PZMO-720, and Pd/ZMO-30 are similar, confirming that their active sites have the same properties. Indeed, the DRIFTS results of CO adsorption (Fig. 2F, G, Fig. S14, and S15) indicate that they all have a similar perfect Pd₃O₄. In contrast, we are not surprised to find that PZMO-30 can oxidize CO efficiently at room temperature, evidenced by a significantly lower T₉₀ value of 26 °C as compared to about 203 °C for Pd/ZMO-30, validating the conjecture in the DRIFTS results of CO adsorption (Fig. 2H). The apparent activation energy of PZMO-30 is much lower than that of other catalysts, indicating a lower CO oxidation activation barrier of PZMO-30 and different CO oxidation mechanisms. Besides, the turnover frequency (TOF) of PZMO-30 is higher than those of recently reported Pd-based SACs as listed in Table S8. The above results demonstrate that the heterostructured support can efficiently activate Pd²⁺ single atoms in the lattice (the formation of distorted Pd₃O₄, Pd₃O₅, and Pd₃O₃), while similar activation does not exist in Pd/ZMO-30 with Pd²⁺ single atoms dispersed on the surface. Besides, some clusters or nanoparticles exist in Pd/ZMO-30 (Fig. S15) synthesized using the incipient wet impregnation method, which also proves the superiority of the embedded single atoms

in this work. Just as importantly, PZMO-30 also shows excellent cycling stability as no deactivation in low-temperature CO oxidation is observed after repeated light-off measurements (PZMO-30-5th, shown in Fig. 4B). Fig. 6A shows that, after 50 h of the CO oxidation reaction at 30 °C, the CO conversion decreases by about 1.4%; subsequently, full conversion is maintained at 50 °C for 10 h, indicating that PZMO-30 embodies remarkable catalytic stability. Moreover, the effect of H₂O on the activity of CO oxidation is negligible (Fig. 6B and G). The apparent activation energy (E_a) of CO oxidation (Fig. 6H and Fig. S16) slightly increases from 34.87 kJ·mol⁻¹ to 35.46 kJ·mol⁻¹ after the introduction of 2 vol% H₂O (saturated vapor pressure limit), indicating that PZMO-30 has excellent catalytic stability and water resistance, and shows potential for industrial applications.

In situ DRIFTS of CO oxidation are conducted to reveal the structure-activity relationship of PZMO-30 and PZMO. Fig. 4D shows that PZMO-30 can stably catalyze CO oxidation at 25 °C, as evidenced by the gradual increase and eventual stabilization of the CO₂ peak intensity with time. The presence of O₂ reduces the generation of Pd₃O₃, as demonstrated by the peak at 2169 cm⁻¹ shifting only to 2180 cm⁻¹, not to 2185 cm⁻¹ when CO/He is passed through. During the gradual heating process (Fig. 4E), from 25 °C to 60 °C, the peak intensity at

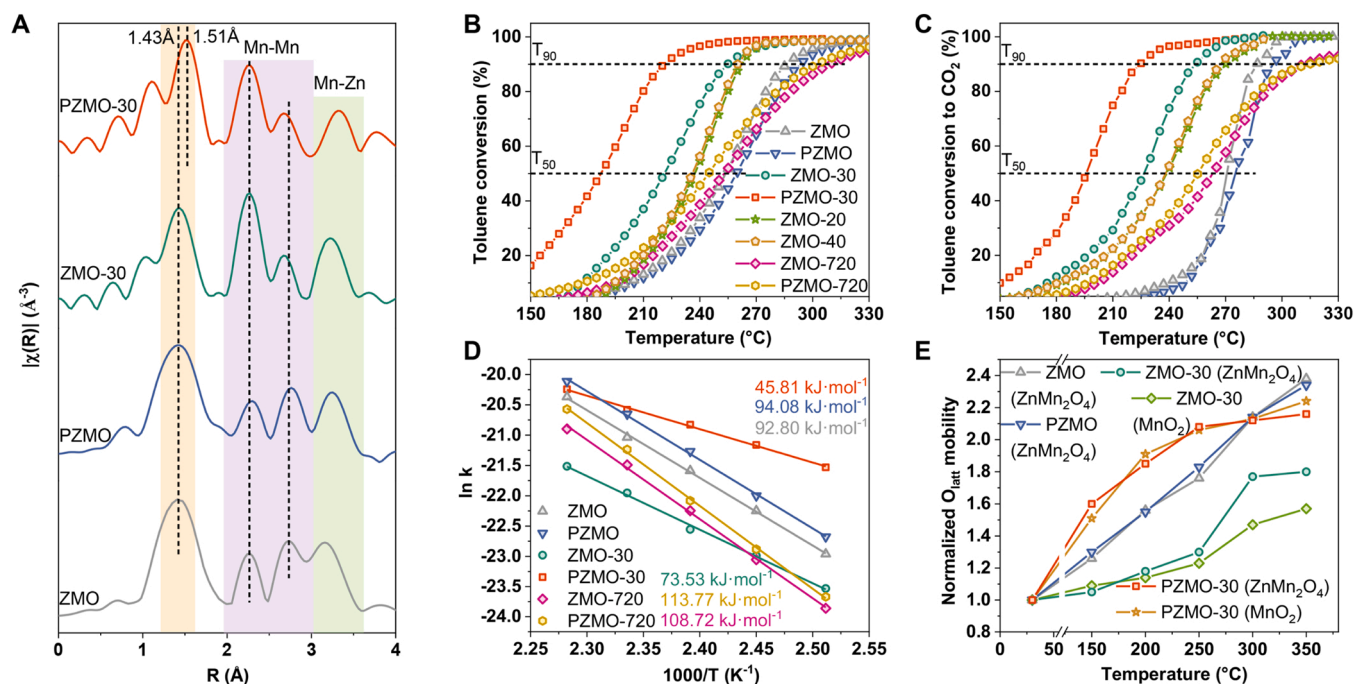


Fig. 5. The effect of the strong MSIs on the heterostructured support. (A) Fourier-transformed K-edge EXAFS spectra in the R-space of Mn. (B) Catalytic performance of toluene oxidation. (C) Toluene conversion to CO₂ as a function of temperature. Reaction conditions: A catalyst loading of 100 mg, and 1000 ppm toluene in synthetic air with a total flow rate of 100 mL·min⁻¹ under a GHSV of 60000 mL·g⁻¹·h⁻¹. (D) Arrhenius plots of the catalysts. (E) Normalized Raman intensities of different phases as a function of temperature. The process of normalizing the Raman signal intensity was done by dividing the peak area of the respective phase at 30 °C by the peak area of the respective phase at other temperatures.

2180 cm⁻¹ is enhanced and shifts to 2182 cm⁻¹, but the peak intensity at 2121 cm⁻¹ is slightly weakened, which indicates that moderately elevated temperature promotes the reduction of distorted Pd₁O₄ to Pd₁O₃. The gradual increase in the CO₂ peak intensity from 60 °C to 180 °C suggests an increasing reaction rate, while the gradual shift of the peak at 2182 cm⁻¹ to lower wavenumbers from 60 °C to 150 °C indicates a decrease in Pd₁O₃ and an enhancement of its ability to activate O₂ to form Pd₁O₅. Subsequently, in Fig. 4F, we turn off CO and observe the catalytic behavior of PZMO-30 in the O₂/He atmosphere at 120 °C. The high peak intensity of CO₂ indicates that the adsorbed CO is catalytically oxidized rather than purged away. During the weakening of the CO peak intensity caused by O₂/He purging, three significant peaks (located at 2185, 2153, and 2121 cm⁻¹) are found (inset in Fig. 4F). This suggests that the peak at 2169 cm⁻¹ results from the overlapping of the peaks at 2185 cm⁻¹ and 2153 cm⁻¹. Based on the above results that the activation of O₂ by Pd₁O₃ to form Pd₁O₅ leads to a shift of CO adsorption to lower wavenumbers, the peak at 2153 cm⁻¹ should be attributed to Pd₁O₅.

As shown in Fig. 4G, in the heterostructured support with rich O_{vac}, Pd²⁺ single atoms are connected to O_{vac} to form coordinatively unsaturated Pd₁O₃, which can activate O₂ to form Pd₁O₅; besides, the ZnMn₂O₄@MnO₂ heterostructure induces distorted Pd₁O₄, which weakens the strength of Pd-O bond, so that it is easier to be reduced by CO to form Pd₁O₃, and Pd₁O₃ can further activate O₂ to form Pd₁O₅. At room temperature without O₂, CO reduces all Pd₁O₅ and a portion of distorted Pd₁O₄ to Pd₁O₃. In the presence of O₂, CO reduces a portion of Pd₁O₅ and distorted Pd₁O₄ to Pd₁O₃ while Pd₁O₃ can activate O₂ to form Pd₁O₅, which facilitates stable CO oxidation. Upon gradual heating with O₂, more Pd₁O₅ and distorted Pd₁O₄ are reduced to Pd₁O₃ by CO. As the temperature increases further, the ability of Pd₁O₃ to activate O₂ improves significantly, resulting in the increase of Pd₁O₅ and the reaction rate. Regarding the reaction mechanism of PZMO-30, CO first reduces distorted Pd₁O₄ to Pd₁O₃, then Pd₁O₃ and Pd₁O₅ form an efficient redox pair, so PZMO-30 follows the "MvK-induced Langmuir-Hinshelwood (L-H) mechanism".

For PZMO, Fig. S17 shows the in situ DRIFTS of CO oxidation at 25 °C. Similar to the DRIFTS results under the CO/He atmosphere (Fig. 2F), almost no CO₂ is produced, indicating that the perfect Pd₁O₄ has little catalytic activity at room temperature. During gradual heating (Fig. 4H), the spectra remain almost constant between 25 °C and 60 °C. At 90 °C, the intensity of the peak at 2170 cm⁻¹ decreases and shifts to higher wavenumbers, indicating the reduction of perfect Pd₁O₄ and the formation of Pd₁O₃, while a new peak (Pd₁O₅) emerges at 2153 cm⁻¹. The intensity of the Pd₁O₅ peak increases with temperature, and between 90 and 180 °C, the peak near 2170 cm⁻¹ continues to shift to higher wavenumbers, indicating the reduction of more perfect Pd₁O₄ to Pd₁O₃. Meanwhile, Pd₁O₃ activating O₂ to form Pd₁O₅ causes the accumulation of Pd₁O₅. The accumulation of Pd₁O₅ suggests that the reactivity of Pd₁O₃ and Pd₁O₅ formed by reducing perfect Pd₁O₄ is low. Fig. S18 shows that the peak at 2179 cm⁻¹ shifts to higher wavenumbers over time and ultimately reaches 2185 cm⁻¹ in the O₂/He atmosphere at 120 °C, indicating the reduction of more perfect Pd₁O₄ to Pd₁O₃. Meanwhile, the accumulated Pd₁O₅ (2153 cm⁻¹) exhibits negligible participation in the reaction. These findings confirm that CO oxidation at 120 °C follows the MvK mechanism. Notably, the low CO₂ peak intensity implies that the adsorbed CO is primarily purged away rather than oxidized. Regarding PZMO, at room temperature, the absence or presence of O₂ results in similar outcomes: CO adsorbs onto perfect Pd₁O₄, and catalyzing CO oxidation is almost impossible. Upon gradual heating in the presence of O₂, perfect Pd₁O₄ is not reduced by CO until 90 °C to form Pd₁O₃ and Pd₁O₅. However, the Pd₁O₃ and Pd₁O₅ resulting from the reduction of perfect Pd₁O₄ exhibit low reactivity, leading to the accumulation of Pd₁O₃ and Pd₁O₅ and low catalytic activity in CO oxidation.

PZMO does not have sufficient O_{vac}, so there is no Pd₁O₅ and Pd₁O₃ at low temperatures. The Pd₁O₃ and Pd₁O₅ formed by reducing perfect Pd₁O₄ are hardly reactive at elevated temperatures. In contrast, PZMO-30 possesses abundant O_{vac} and a distorted Pd₁O₄ due to the ZnMn₂O₄@MnO₂ heterostructure. The abundant O_{vac} results in the presence of Pd₁O₃ in PZMO-30, and the Pd-O bond strength of distorted

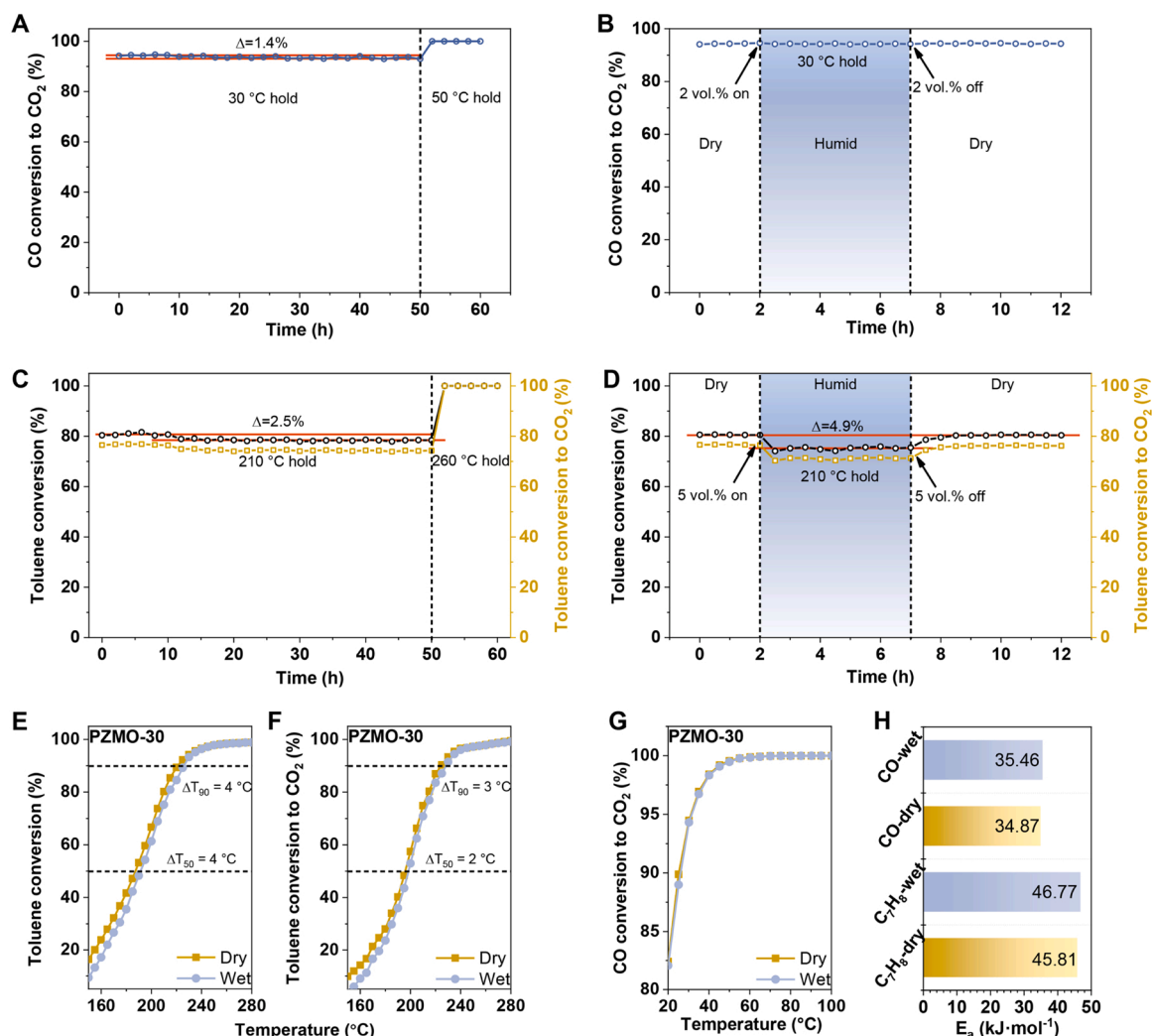


Fig. 6. Catalytic stability and water resistance of PZMO-30. (A) Catalyst stability and (B) water resistance for CO oxidation of PZMO-30. Reaction condition: a catalyst loading of 100 mg, 1% CO, 20% O₂, and 2 vol% H₂O (when used) in N₂ with a total flow rate of 100 mL·min⁻¹ under a GHSV of 60000 mL·g⁻¹·h⁻¹. (C) Catalyst stability and (D) water resistance for toluene oxidation of PZMO-30. Reaction condition: a catalyst loading of 100 mg, 1000 ppm toluene, and 5 vol% H₂O (when used) in synthetic air with a total flow rate of 100 mL·min⁻¹ under a GHSV of 60000 mL·g⁻¹·h⁻¹. (E) & (F) The catalytic performance of toluene oxidation over PZMO-30 without H₂O and with 5 vol% H₂O. (G) The catalytic performance of CO oxidation over PZMO-30 without H₂O and with 2 vol% H₂O. (H) The apparent activation energy of PZMO-30 for CO and toluene (C₇H₈) oxidation under dry and wet conditions.

Pd₁O₄ is lower than that of perfect Pd₁O₄, facilitating its reduction by CO to form Pd₁O₃. The combination of Pd₁O₃ and Pd₁O₅ forms an active redox pair that efficiently catalyzes CO oxidation even at room temperature. This supports the superiority of the "MvK-induced L-H mechanism" over the MvK mechanism alone.

3.4. MSIs effect on support O_{latt}

The EXAFS results at Mn K-edge (Fig. 5A) indicate that the Mn-O bond lengths of ZMO, PZMO, and ZMO-30 are all 1.43 Å, while PZMO-30 has an elongated Mn-O with a bond length of 1.51 Å. PZMO does not possess elongated Mn-O, indicating that perfect Pd₁O₄ does not cause the elongated Mn-O bonds; ZMO-30 does not possess elongated Mn-O, indicating that the ZnMn₂O₄@MnO₂ heterostructure is not the cause either for the elongated Mn-O bonds. Therefore, the elongated Mn-O bonds of PZMO-30 should be attributed to its unique Pd²⁺ single atoms (or the heterostructure-strengthened MSIs), i.e., distorted Pd₁O₄, Pd₁O₃, and Pd₁O₅.

The elongated Mn-O bond may further facilitate the activation of O_{latt} to participate in the deep oxidation of VOCs. Therefore, we choose toluene, a stable VOC that requires O_{latt} to participate in its catalytic

removal,[44] as the probe molecule to test the catalytic performance of deep oxidation, and the activity results are shown in Fig. 5B, C, and Table S7. The activity of ZMO-30 is higher than that of ZMO-20 and ZMO-40, which proves that an acid treatment time of 30 min gives the best properties of the ZnMn₂O₄@MnO₂ heterostructure. The ZnMn₂O₄@MnO₂ heterostructure enhances catalytic activity through the interface effects between ZnMn₂O₄ and MnO₂ shown in Fig. 3A. The activity of PZMO-720 is only slightly higher than that of ZMO-720, and that of PZMO is even slightly lower than that of ZMO. This suggests that a perfect Pd₁O₄ cannot activate the O_{latt} of the support. On the contrary, the activity of PZMO-30 is significantly increased compared to ZMO-30. This should be attributed to the activation effect of unique Pd²⁺ single atoms on the O_{latt} of the support in PZMO-30. Additionally, the curve of toluene conversion to CO₂ (Fig. 5C) closely follows that of toluene conversion (Fig. 5B), with CO₂ selectivity exceeding 93% at 210 °C and increasing with temperature (Fig. S19). This suggests that toluene is efficiently converted to harmless CO₂ and H₂O via deep oxidation. The corresponding Arrhenius plots are shown in Fig. 5D. The perfect Pd₁O₄ in PZMO and PZMO-720 cannot reduce the apparent activation energy compared to ZMO and ZMO-720, respectively. In contrast, the unique Pd²⁺ single atoms of PZMO-30 significantly reduce the apparent

activation energy compared to ZMO-30, indicating that only the unique Pd^{2+} single atoms are capable of activating the O_{latt} of the support. Compared with the reported catalysts, PZMO-30 is among those with one of the lowest apparent activation energies for toluene oxidation as listed in Table S9. Fig. 6C illustrates that the toluene conversion of PZMO-30 decreases by approximately 2.5% after 50 h of reaction at 210 °C, then it maintains full conversion at 260 °C for 10 h, indicating the remarkable catalytic stability of PZMO-30. Fig. 6D shows that the introduction of 5 vol% H_2O results in a decrease of only 4.9% in toluene conversion. Moreover, the toluene conversion quickly recovers to its original level once the water vapor is removed, indicating that PZMO-30 is not susceptible to being poisoned by additional hydroxyl derived from water vapor and that the impact of water vapor is entirely reversible. The weak effect of H_2O on the light-off curve (Fig. 6E and F) and the apparent activation energy (E_a , Fig. 6H and Fig. S16) of toluene oxidation confirms the outstanding catalytic stability and water resistance of PZMO-30.

Subsequently, we employ in situ Raman technique to further determine the O_{latt} contribution and reveal the O_{latt} activity of different phases in the support. The in situ Raman spectra of toluene adsorption at 30 °C and the corresponding Raman signal attributions are presented in Fig. S20. Fig. S21 displays the in situ Raman spectra of toluene oxidation during the gradual heating process. The temperature-dependent changes in peak intensity are attributed to the motion of O_{latt} between the sub-surface and bulk, which results from a reversible redox reaction between $\text{Mn}^{4+}/\text{Mn}^{3+}/\text{Mn}^{2+}$ under the influence of the reducing molecule (toluene). [47,48] Therefore, the reduction in peak intensity after heating confirms that O_{latt} participates in the deep oxidation of toluene, and the O_{latt} activity is very important for the low-temperature activity towards toluene oxidation. The normalized Raman intensities can represent the O_{latt} activity of different phases at varying temperatures. [49,50] As shown in Fig. 5E, ZMO and PZMO have similar O_{latt} activities, suggesting that the O_{latt} of ZnMn_2O_4 is unaffected by perfect Pd_1O_4 , which is consistent with the O_2 -TPD results (Fig. 3D). The O_{latt} activity of MnO_2 of ZMO-30 is significantly lower than that of ZnMn_2O_4 of ZMO and PZMO, indicating that the higher catalytic activity of ZMO-30 compared to ZMO is not due to the formation of MnO_2 but is related to the $\text{ZnMn}_2\text{O}_4@/\text{MnO}_2$ heterostructure. In other words, the presence of MnO_2 alone cannot increase the activity, which is consistent with the low activity of ZMO-720. The lower O_{latt} activity of ZnMn_2O_4 of ZMO-30 relative to ZMO and PZMO should be attributed to the lower Raman sensitivity of ZnMn_2O_4 located in the core of the core-shell structure. In contrast, the low-temperature O_{latt} activity of PZMO-30 (ZnMn_2O_4 and MnO_2 , ≤ 250 °C) is significantly higher than that of the other three samples, indicating that only the unique Pd^{2+} single atoms in the lattice can enhance the O_{latt} activity.

To further understand the effect of the unique Pd^{2+} single atoms on O_{latt} from a mechanism point of view, in situ DRIFTS studies of toluene oxidation are employed. All the identified bands and related species are summarized in Table S10. Fig. S22 shows the toluene adsorption states at room temperature. The hydroxyl group (-OH) is formed through the methyl dehydrogenation of toluene, and the -OH signal of PZMO-30 is the strongest, indicating that PZMO-30 has the most robust dehydrogenation ability at room temperature. As toluene exposure time increases for ZMO, PZMO, ZMO-30, and PZMO-30, the signal intensity of benzene ring increases, demonstrating the adsorption of toluene on the catalyst surface. Peaks of intermediate species such as benzaldehyde, benzoate, phenolate, and benzyl alcohol are also observed, indicating a plausible reaction pathway on the four catalysts at room temperature: toluene \rightarrow benzyl alcohol \rightarrow benzaldehyde \rightarrow benzoic acid \rightarrow phenol. Furthermore, a benzoquinone signal appears on ZMO-30 and PZMO-30, and a new adsorption peak of maleic anhydride (936 cm^{-1}) is present on PZMO-30. The $\text{ZnMn}_2\text{O}_4@/\text{MnO}_2$ heterostructure of ZMO-30 and PZMO-30 facilitates the further oxidation of phenol to benzoquinone. The unique Pd^{2+} single atoms of PZMO-30 enhance the activity of O_{latt} , promoting the cleavage of benzene ring (i.e., the oxidation of

benzoquinone to maleic anhydride). Therefore, there may be a reaction pathway in PZMO-30 at room temperature: phenol \rightarrow benzoquinone \rightarrow maleic anhydride. Fig. S23 shows the toluene oxidation mechanism versus temperature. Formate species are observed at 1558 cm^{-1} for ZMO, PZMO, and ZMO-30 between 150 °C and 350 °C, while in PZMO-30, formate species exist only in the range of 150–200 °C. This suggests that PZMO-30 exhibits higher O_{latt} activity, leading to better oxidation of formate. The resulting carbonate species (1529 cm^{-1}) from formate oxidation appear at 150 °C. The carbonate species of ZMO persist up to 250 °C, whereas those of the other catalysts disappear at 200 °C, indicating a slower decomposition rate of carbonate species on ZMO. Moreover, the peak intensity of maleic anhydride in PZMO-30 increases rapidly as the temperature increases, with the final intensity being the highest. This confirms the high O_{latt} activity of PZMO-30 induced by the unique Pd^{2+} single atoms, promoting the cleavage of benzene ring. Therefore, it is proposed that PZMO-30 may follow the reaction pathway of maleic anhydride \rightarrow formic acid \rightarrow carbonate \rightarrow CO_2 at elevated temperatures.

4. Conclusions

In conclusion, we have developed a facile yet efficient method to tune the MSIs of single-atom Pd catalysts, resulting in the improved activity of oxygen species (O_{ads} and O_{latt}) for the catalytic oxidation of CO and toluene. By forming heterostructures ($\text{ZnMn}_2\text{O}_4@/\text{MnO}_2$) in the support, the MSIs between the embedded Pd^{2+} single atoms and support are strengthened. This optimizes the coordination configuration of Pd^{2+} single atoms, significantly improving the molecular oxygen activation ability of the catalyst, which benefits CO oxidation and gives rise to a novel "MvK-induced L-H" reaction mechanism. Additionally, the unique Pd^{2+} single atoms induce the stretching of the Mn-O bond, enhancing O_{latt} mobility and lowering the energy barrier for toluene oxidation. Our work proposes that highly reactive oxygen species can be facilely obtained by burying noble metal single atoms in the support lattice and inducing the formation of heterostructures. Importantly, we believe that this method may be expanded as the family of heterostructured materials is continually enriched, opening up new avenues for promoting various oxidation reactions.

CRedit authorship contribution statement

Bin Wang: Conceptualization, Methodology, Validation, Formal analysis, Investigation, Software, Visualization, Writing - original draft. **Qilei Yang:** Methodology, Formal analysis. **Bing Li:** Methodology. **Hongyuan Ma:** Writing - original draft. **Yue Xuan:** Investigation. **Chuan Gao:** Methodology. **Yanjie Liang:** Software. **Kaihang Zhang:** Visualization. **Qiaowan Chang:** Writing - review & editing. **Osvaldo Broesicke:** Visualization. **Houlin Wang:** Investigation. **Dong Wang:** Conceptualization, Supervision, Project administration, Funding acquisition, Investigation, Writing - review & editing. **Tao Luan:** Writing - review & editing. **Kuihua Han:** Writing - review & editing. **Chunmei Lu:** Writing - review & editing, Supervision. **John Crittenden:** Supervision.

Declaration of Competing Interest

The authors declare that they have no known competing financial interests or personal relationships that could have appeared to influence the work reported in this paper.

Data Availability

Data will be made available on request.

Acknowledgements

This work was financially supported by the National Natural Science Foundation of China (22276111). The authors appreciate the support from the SDU-ZMDE Joint Laboratory for Environmental Protection and Energy Saving, the National Engineering Laboratory for Coal-Burning Pollutants Emission Reduction, and the Brook Byers Institute for Sustainable Systems, Hightower Chair and Georgia Research Alliance at the Georgia Institute of Technology. The views and ideas expressed herein are solely those of the authors and do not represent the opinions of the funding agencies in any form.

Associated Content

N/A.

Supporting Information

Detailed experimental procedures, attribution of reduction peaks, XRD patterns, XPS spectra, in situ pyridine-FTIR spectra, NH₃-TPD profiles, TEM images, AC-STEM images, EXAFS fitting curves, EELS spectra, in situ DRIFTS spectra, in situ Raman spectra, textural properties of catalysts, the best fitting results of EXAFS, catalytic performance, assignment of the in situ DRIFTS bands, and supplementary references are included.

Appendix A. Supporting information

Supplementary data associated with this article can be found in the online version at [doi:10.1016/j.apcatb.2023.122753](https://doi.org/10.1016/j.apcatb.2023.122753).

References

- M.M. Montemore, M.A. van Spronsen, R.J. Madix, C.M. Friend, O₂ Activation by metal surfaces: implications for bonding and reactivity on heterogeneous catalysts, *Chem. Rev.* 118 (2018) 2816–2862, <https://doi.org/10.1021/acs.chemrev.7b00217>.
- D. Mukherjee, A. Ellern, A.D. Sadow, Remarkably robust monomeric alkylperoxyzinc compounds from tris(oxazolonyl)boratozinc alkyls and O₂, *J. Am. Chem. Soc.* 134 (2012) 13018–13026, <https://doi.org/10.1021/ja303440n>.
- Y. Ma, L. Wang, J. Ma, H. Wang, C. Zhang, H. Deng, H. He, Investigation into the enhanced catalytic oxidation of o-Xylene over MOF-derived Co₃O₄ with different shapes: the role of surface twofold-coordinate lattice oxygen (O₂), *ACS Catal.* 11 (2021) 6614–6625, <https://doi.org/10.1021/acscatal.1c01116>.
- H. Li, S. Kelly, D. Guevarra, Z. Wang, Y. Wang, J.A. Haber, M. Anand, G.T.K. K. Gunasooriya, C.S. Abraham, S. Vijay, J.M. Gregoire, J.K. Nørskov, Analysis of the limitations in the oxygen reduction activity of transition metal oxide surfaces, *Nat. Catal.* 4 (2021) 463–468, <https://doi.org/10.1038/s41929-021-00618-w>.
- B. Wang, J. Ma, D. Wang, Z.Q. Gong, Q.L. Shi, C.A. Gao, C.M. Lu, J. Crittenden, Acid-pretreated red mud for selective catalytic reduction of NO_x with NH₃: Insights into inhibition mechanism of binders, *Catal. Today* 376 (2021) 247–254, <https://doi.org/10.1016/j.cattod.2020.05.036>.
- X. Liu, J. Mi, L. Shi, H. Liu, J. Liu, Y. Ding, J. Shi, M. He, Z. Wang, S. Xiong, Q. Zhang, Y. Liu, Z.S. Wu, J. Chen, J. Li, In situ modulation of A-site vacancies in LaMnO_{3.15} perovskite for surface lattice oxygen activation and boosted redox reactions, *Angew. Chem. Int. Ed.* 60 (2021) 26747–26754, <https://doi.org/10.1002/anie.202111610>.
- J. Yang, S. Hu, Y. Fang, S. Hoang, L. Li, W. Yang, Z. Liang, J. Wu, J. Hu, W. Xiao, C. Pan, Z. Luo, J. Ding, L. Zhang, Y. Guo, Oxygen vacancy promoted O₂ activation over perovskite oxide for low-temperature CO oxidation, *ACS Catal.* 9 (2019) 9751–9763, <https://doi.org/10.1021/acscatal.9b02408>.
- J.X. Liu, Y. Su, I.A.W. Pilot, E.J.M. Hensen, A linear scaling relation for CO oxidation on CeO₂-supported Pd, *J. Am. Chem. Soc.* 140 (2018) 4580–4587, <https://doi.org/10.1021/jacs.7b13624>.
- A.R. Puigdollers, G. Pacchioni, CO oxidation on Au nanoparticles supported on ZrO₂: role of metal/oxide interface and oxide reducibility, *ChemCatChem* 9 (2017) 1119–1127, <https://doi.org/10.1002/cctc.201601486>.
- H. Gu, X. Liu, X. Liu, C. Ling, K. Wei, G. Zhan, Y. Guo, L. Zhang, Adjacent single-atom irons boosting molecular oxygen activation on MnO₂, *Nat. Commun.* 12 (2021) 5422, <https://doi.org/10.1038/s41467-021-25726-w>.
- Z. Hu, X. Liu, D. Meng, Y. Guo, Y. Guo, G. Lu, Effect of ceria crystal plane on the physicochemical and catalytic properties of Pd/Ceria for CO and propane oxidation, *ACS Catal.* 6 (2016) 2265–2279, <https://doi.org/10.1021/acscatal.5b02617>.
- B. Qiao, A. Wang, X. Yang, L.F. Allard, Z. Jiang, Y. Cui, J. Liu, J. Li, T. Zhang, Single-atom catalysis of CO oxidation using Pt₁/FeO_x, *Nat. Chem.* 3 (2011) 634–641, <https://doi.org/10.1038/NCHEM.1095>.
- Z. Zhou, Q. Shen, K. Yuan, W. Yang, Q. Chen, Z. Geng, J. Zhang, X. Shao, W. Chen, G. Xu, X. Yang, K. Wu, Unraveling charge state of supported Au single-atoms during CO oxidation, *J. Am. Chem. Soc.* 140 (2018) 554–557, <https://doi.org/10.1021/jacs.7b10394>.
- Y. Chen, J. Gao, Z. Huang, M. Zhou, J. Chen, C. Li, Z. Ma, J. Chen, X. Tang, Sodium rivals silver as single-atom active centers for catalyzing abatement of formaldehyde, *Environ. Sci. Technol.* 51 (2017) 7084–7090, <https://doi.org/10.1021/acs.est.7b00499>.
- Y. Shi, Z.R. Ma, Y.Y. Xiao, Y.C. Yin, W.M. Huang, Z.C. Huang, Y.Z. Zheng, F.Y. Mu, R. Huang, G.Y. Shi, Y.Y. Sun, X.H. Xia, W. Chen, Electronic metal-support interaction modulates single-atom platinum catalysis for hydrogen evolution reaction, *Nat. Commun.* 12 (2021) 3021, <https://doi.org/10.1038/s41467-021-23306-6>.
- L. Liu, A. Corma, Metal catalysts for heterogeneous catalysis: from single atoms to nanoclusters and nanoparticles, *Chem. Rev.* 118 (2018) 4981–5079, <https://doi.org/10.1021/acs.chemrev.7b00776>.
- E. Sasmaz, C. Wang, M.J. Lance, J. Lauterbach, In situ spectroscopic investigation of a Pd local structure over Pd/CeO₂ and Pd/MnO_x-CeO₂ during CO oxidation, *J. Mater. Chem. A* 5 (2017) 12998–13008, <https://doi.org/10.1039/c7ta00696a>.
- C. Wang, C. Wen, J. Lauterbach, E. Sasmaz, Superior oxygen transfer ability of Pd/MnO_x-CeO₂ for enhanced low temperature CO oxidation activity, *Appl. Catal. B* 206 (2017) 1–8, <https://doi.org/10.1016/j.apcatb.2017.01.020>.
- X.I. Pereira-Hernández, A. DeLaRiva, V. Muravev, D. Kunwar, H. Xiong, B. Sudduth, M. Engelhard, L. Kovarik, E.J.M. Hensen, Y. Wang, A.K. Datye, Tuning Pt-CeO₂ interactions by high-temperature vapor-phase synthesis for improved reducibility of lattice oxygen, *Nat. Commun.* 10 (2019) 1358, <https://doi.org/10.1038/s41467-019-09308-5>.
- A.M. Gänzler, M. Casapu, P. Vernoux, S. Lorient, F.J. Cadete Santos Aires, T. Epicer, B. Betz, R. Hoyer, J.D. Grunwaldt, Tuning the structure of platinum particles on ceria in situ for enhancing the catalytic performance of exhaust gas catalysts, *Angew. Chem. Int. Ed.* 56 (2017) 13078–13082, <https://doi.org/10.1002/anie.201707842>.
- A.M. Gänzler, M. Casapu, F. Maurer, H. Störmer, D. Gerthsen, G. Ferré, P. Vernoux, B. Bornmann, R. Frahm, V. Murzin, M. Nachttegaal, M. Votsmeier, J.D. Grunwaldt, Tuning the Pt/CeO₂ interface by in situ variation of the Pt particle size, *ACS Catal.* 8 (2018) 4800–4811, <https://doi.org/10.1021/acscatal.8b00330>.
- H. Wang, J.X. Liu, L.F. Allard, S. Lee, J. Liu, H. Li, J. Wang, J. Wang, S.H. Oh, W. Li, M. Flytzani-Stephanopoulos, M. Shen, B.R. Goldsmith, M. Yang, Surpassing the single-atom catalytic activity limit through paired Pt-O-Pt ensemble built from isolated Pt₁ atoms, *Nat. Commun.* 10 (2019) 3808, <https://doi.org/10.1038/s41467-019-11856-9>.
- R. Kopelent, J.A. van Bokhoven, J. Szlachetko, J. Edebeli, C. Paun, M. Nachttegaal, O.V. Safonova, Catalytically active and spectator Ce³⁺ in ceria-supported metal catalysts, *Angew. Chem. Int. Ed.* 54 (2015) 8728–8731, <https://doi.org/10.1002/anie.201503022>.
- J. Liu, L. Wang, F. Okejiri, J. Luo, J. Zhao, P. Zhang, M. Liu, S. Yang, Z. Zhang, W. Song, W. Zhu, J. Liu, Z. Zhao, G. Feng, C. Xu, S. Dai, Deep understanding of strong metal interface confinement: a journey of Pd/FeO_x catalysts, *ACS Catal.* 10 (2020) 8950–8959, <https://doi.org/10.1021/acscatal.0c01447>.
- Y. Zhang, Y. Xu, Y. Zhou, S. Xiang, S. Sheng, Q. Wang, C. Zhang, Hierarchical structures based on gold nanoparticles embedded into hollow ceria spheres and mesoporous silica layers with high catalytic activity and stability, *N. J. Chem.* 39 (2015) 9372–9379, <https://doi.org/10.1039/c5nj01990g>.
- S. Colussi, A. Gayen, M. Farnesi Camellone, M. Boaro, J. Llorca, S. Fabris, A. Trovarelli, Nanofaceted Pd-O Sites in Pd-Ce surface superstructures: enhanced activity in catalytic combustion of methane, *Angew. Chem. Int. Ed.* 48 (2009) 8481–8484, <https://doi.org/10.1002/anie.200903581>.
- J. Xiong, J. Yang, X. Chi, K. Wu, L. Song, T. Li, Y. Zhao, H. Huang, P. Chen, J. Wu, L. Chen, M. Fu, D. Ye, Pd-promoted Co₂NiO₄ with lattice CoONi and interfacial PdO activation for highly efficient methane oxidation, *Appl. Catal. B* 292 (2021), 120201, <https://doi.org/10.1016/j.apcatb.2021.120201>.
- J. Li, Q. Guan, H. Wu, W. Liu, Y. Lin, Z. Sun, X. Ye, X. Zheng, H. Pan, J. Zhu, S. Chen, W. Zhang, S. Wei, J. Lu, Highly active and stable metal single-atom catalysts achieved by strong electronic metal-support interactions, *J. Am. Chem. Soc.* 141 (2019) 14515–14519, <https://doi.org/10.1021/jacs.9b06482>.
- L. DeRita, J. Resasco, S. Dai, A. Boubnov, H.V. Thang, A.S. Hoffman, I. Ro, G. W. Graham, S.R. Bare, G. Pacchioni, X. Pan, P. Christopher, Structural evolution of atomically dispersed Pt catalysts dictates reactivity, *Nat. Mater.* 18 (2019) 746–751, <https://doi.org/10.1038/s41563-019-0349-9>.
- M. Yoo, Y.S. Yu, H. Ha, S. Lee, J.S. Choi, S. Oh, E. Kang, H. Choi, H. An, K.S. Lee, J. Y. Park, R. Celestre, M.A. Marcus, K. Nowrouzi, D. Taube, D.A. Shapiro, W. Jung, C. Kim, H.Y. Kim, A tailored oxide interface creates dense Pt single-atom catalysts with high catalytic activity, *Energy Environ. Sci.* 13 (2020) 1231–1239, <https://doi.org/10.1039/c9ee03492g>.
- L. Li, Q. Yang, D. Wang, Y. Peng, J. Yan, J. Li, J. Crittenden, Facile synthesis •-MnO₂ spinel for highly effective catalytic oxidation of benzene, *Chem. Eng. J.* 421 (2021), 127828, <https://doi.org/10.1016/j.cej.2020.127828>.
- J. Yang, S. Hu, L. Shi, S. Hoang, W. Yang, Y. Fang, Z. Liang, C. Pan, Y. Zhu, L. Li, J. Wu, J. Hu, Y. Guo, Oxygen vacancies and lewis acid sites synergistically promoted catalytic methane combustion over perovskite oxides, *Environ. Sci. Technol.* 55 (2021) 9243–9254, <https://doi.org/10.1021/acs.est.1c00511>.

- [33] M.M. Natile, E. Ugel, C. Maccato, A. Glisenti, LaCoO_3 : effect of synthesis conditions on properties and reactivity, *Appl. Catal. B.* 72 (2007) 351–362, <https://doi.org/10.1016/j.apcatb.2006.11.011>.
- [34] B. Wang, G. Yang, Q. Yang, B. Li, D. Wang, Y. Peng, J. Li, C. Lu, J. Crittenden, Fabrication of nanohybrid Spinel@CuO catalysts for propane oxidation: modified spinel and enhanced activity by temperature-dependent acid sites, *ACS Appl. Mater. Interfaces* 13 (2021) 27106–27118, <https://doi.org/10.1021/acsami.1c06633>.
- [35] G. Wang, L. Wang, X. Fei, Y. Zhou, R.F. Sabirianov, W.N. Mei, C.L. Cheung, Probing the bifunctional catalytic activity of ceria nanorods towards the cyanosilylation reaction, *Catal. Sci. Technol.* 3 (2013) 2602–2609, <https://doi.org/10.1039/c3cy00196b>.
- [36] D. Jiang, G. Wan, C.E. García-Vargas, L. Li, X.I. Pereira-Hernández, C. Wang, Y. Wang, Elucidation of the active sites in single-atom Pd_1/CeO_2 catalysts for low-temperature CO oxidation, *ACS Catal.* 10 (2020) 11356–11364, <https://doi.org/10.1021/acscatal.0c02480>.
- [37] D. Tessier, A. Rakai, F. Bozon-Verduraz, Spectroscopic study of the interaction of carbon monoxide with cationic and metallic palladium in palladium-alumina catalysts, *J. Chem. Soc. Faraday Trans.* 88 (1992) 741–749, <https://doi.org/10.1039/ft9928800741>.
- [38] L. Li, N. Zhang, R. Wu, L. Song, G. Zhang, H. He, Comparative study of moisture-treated $\text{Pd@CeO}_2/\text{Al}_2\text{O}_3$ and $\text{Pd/CeO}_2/\text{Al}_2\text{O}_3$ catalysts for automobile exhaust emission reactions: effect of core-shell interface, *ACS Appl. Mater. Interfaces* 12 (2020) 10350–10358, <https://doi.org/10.1021/acsami.9b20734>.
- [39] A.J. Binder, T.J. Toops, R.R. Unocic, J.E. Parks, I.I. S. Dai, Low-temperature CO oxidation over a ternary oxide catalyst with high resistance to hydrocarbon inhibition, *Angew. Chem. Int. Ed.* 54 (2015) 13263–13267, <https://doi.org/10.1002/anie.201506093>.
- [40] C.D. Zeinalipour-Yazdi, D.J. Willock, L. Thomas, K. Wilson, A.F. Lee, CO adsorption over Pd nanoparticles: a general framework for IR simulations on nanoparticles, *Surf. Sci.* 646 (2016) 210–220, <https://doi.org/10.1016/j.susc.2015.07.014>.
- [41] W.H. Yang, Y. Peng, Y. Wang, Y. Wang, H. Liu, Z.A. Su, W.N. Yang, J.J. Chen, W. Z. Si, J.H. Li, Controllable redox-induced in-situ growth of MnO_2 over Mn_2O_3 for toluene oxidation: active heterostructure interfaces, *Appl. Catal. B.* 278 (2020), 119279, <https://doi.org/10.1016/j.apcatb.2020.119279>.
- [42] X. Liao, Y. Zhao, C. Liu, X. Li, Y. Sun, K. Kato, M. Yamauchi, Z. Jiang, Low temperature surface oxygen activation in crystalline MnO_2 triggered by lattice confined Pd single atoms, *J. Energy Chem.* 62 (2021) 136–144, <https://doi.org/10.1016/j.jechem.2021.03.012>.
- [43] H. Tan, J. Wang, S. Yu, K. Zhou, Support morphology-dependent catalytic activity of Pd/CeO_2 for formaldehyde oxidation, *Environ. Sci. Technol.* 49 (2015) 8675–8682, <https://doi.org/10.1021/acs.est.5b01264>.
- [44] Z. Su, W. Si, H. Liu, S. Xiong, X. Chu, W. Yang, Y. Peng, J. Chen, X. Cao, J. Li, Boosting the catalytic performance of CeO_2 in toluene combustion via the Ce-Ce homogeneous interface, *Environ. Sci. Technol.* 55 (2021) 12630–12639, <https://doi.org/10.1021/acs.est.1c03999>.
- [45] D. Kunwar, S. Zhou, A. DeLaRiva, E.J. Peterson, H. Xiong, X.I. Pereira-Hernández, S.C. Purdy, R. ter Veen, H.H. Brongersma, J.T. Miller, H. Hashiguchi, L. Kovarik, S. Lin, H. Guo, Y. Wang, A.K. Datye, Stabilizing high metal loadings of thermally stable platinum single atoms on an industrial catalyst support, *ACS Catal.* 9 (2019) 3978–3990, <https://doi.org/10.1021/acscatal.8b04885>.
- [46] D. Jiang, Y. Yao, T. Li, G. Wan, X.I. Pereira-Hernández, Y. Lu, J. Tian, K. Khivantsev, M.H. Engelhard, C. Sun, C.E. García-Vargas, A.S. Hoffman, S. R. Bare, A.K. Datye, L. Hu, Y. Wang, Tailoring the local environment of platinum in single-atom Pt_1/CeO_2 catalysts for robust low-temperature CO oxidation, *Angew. Chem. Int. Ed.* 60 (2021) 26054–26062, <https://doi.org/10.1002/anie.202108585>.
- [47] Y. Luo, Y.Q. Deng, W. Mao, X.J. Yang, K. Zhu, J. Xu, Y.F. Han, Probing the surface structure of $\mu\text{-Mn}_2\text{O}_3$ nanocrystals during CO oxidation by operando raman spectroscopy, *J. Phys. Chem. C.* 116 (2012) 20975–20981, <https://doi.org/10.1002/anie.202108585>.
- [48] Y.F. Han, K. Ramesh, L. Chen, E. Widjaja, S. Chilukoti, F. Chen, Observation of the reversible phase-transformation of $\mu\text{-Mn}_2\text{O}_3$ nanocrystals during the catalytic combustion of methane by in situ raman spectroscopy, *J. Phys. Chem. C.* 111 (2007) 2830–2833, <https://doi.org/10.1021/jp0686691>.
- [49] J. Chen, X. Chen, W. Xu, Z. Xu, J. Chen, H. Jia, J. Chen, Hydrolysis driving redox reaction to synthesize Mn-Fe binary oxides as highly active catalysts for the removal of toluene, *Chem. Eng. J.* 330 (2017) 281–293, <https://doi.org/10.1016/j.cej.2017.07.147>.
- [50] D.Y. Wei, M.F. Yue, S.N. Qin, S. Zhang, Y.F. Wu, G.Y. Xu, H. Zhang, Z.Q. Tian, J. F. Li, In situ raman observation of oxygen activation and reaction at platinum-ceria interfaces during CO oxidation, *J. Am. Chem. Soc.* 143 (2021) 15635–15643, <https://doi.org/10.1021/jacs.1c04590>.